Journal of
Materials Chemistry A

Materials for energy and sustainability

Accepted Manuscript

This article can be cited before page numbers have been issued, to do this please use: H. N. Dhandapani, R. Karthikeyan, V. Parey, K. Senthivel, S. Chakraborty, R. B. Balakrishnan and S. Kundu, *J. Mater. Chem. A*, 2025, DOI: 10.1039/D5TA04519C.

ROYAL SOCIETY OF CHEMISTRY

rsc.li/materials-a

View Article Online
DOI: 10.1039/D5TA04519C

Hierarchical 3D-nanoflower LDHs Heterojunction: A Bifunctional Electrocatalyst for Total Water Splitting

Hariharan N Dhandapani,[†‡] Ramya Karthikeyan,[†‡] Vanshree Parey,[□] Kaveri Senthivel,[$] Sudip Chakraborty,[□]* B. Ramesh Babu[†‡]* and Subrata Kundu[†‡]*

[†]*Academy of Scientific and Innovative Research (AcSIR), Ghaziabad-201002, India.*

[‡]*Electrochemical Process Engineering (EPE) Division, CSIR-Central Electrochemical Research Institute (CECRI), Karaikudi-630003, Tamil Nadu, India.*

[□] *Materials Theory for Energy Scavenging (MATES) Lab, Harish-Chandra Research Institute, A CI of Homi Bhabha National Institute (HBNI), Chhatnag Road, Prayagraj, Uttar Pradesh, 211019 India.*

[$] *Kalasalingam Academy of Research and Education, Department of Chemistry, Krishnankoil-626126, Tamil Nadu, India.*

**E-mail:* sudiphys@gmail.com; brbabu@cecri.res.in; skundu@cecri.res.in; kundu.subrata@gmail.com; Phone/Fax: (+ 91) 4565-241487.

Abstract

Hydrogen is a clean energy alternative to conventional hydrocarbons in various applications. Water electrolysis is the fastest and most efficient approach for generating pure hydrogen with zero carbon emissions. Layered double hydroxide (LDHs) is the most prominent material for developing efficient and cost-effective electrocatalysts for water splitting. A highly efficient approach for designing an electrocatalyst with improved performance is to develop a hierarchical LDHs heterojunction with a modulating electronic structure. In this work, we designed a hierarchical NiFe-LDH/NiCo-LDHs heterostructure over Ni foam via a hydrothermal process, which exhibits enhanced OER and HER performance in alkaline conditions. Additionally, the heterostructure shows a high faradaic efficiency value of 93.4% at 1.65 V potential, demonstrating excellent selectivity toward electrocatalytic reaction. Furthermore, the prolonged stability over 60 h at 1.55 V highlights its sturdiness. The prepared catalyst exhibits TOF value (0.155 sec^{-1}) that is 13 and 24 times greater than that of NiFe-LDH

(0.0125 sec^{-1}) and NiCo-LDH (0.0063 sec^{-1}), respectively, towards OER. The pH-dependent study reveals that the NiFe-LDH/NiCo-LDH heterostructure follows the Adsorbate enhancement mechanism (AEM) rather than the lattice oxygen mechanism (LOM). DFT studies further confirm the synergistic interaction in the NiFe-LDH/NiCo-LDH interface which facilitates the enhanced activity in OER, whereas in HER the reduction in ΔG_H^* value which increases the adsorption and desorption process of H atom over the catalyst. This work offers a new route for improving electrocatalytic performance by developing the hierarchical LDHs heterojunction.

Keywords: LDH, Impedance, Turnover Frequency, Faradic efficiency, Density of State.

Introduction

Energy consumption heavily relies on carbonaceous fossil fuels like oil, coal, and petrol.[1] The extensive combustion of these fuels has led to global warming, climate issues, and pollution due to CO_2, SO_x, and NO_x emissions.[2–4] Researchers are seeking for clean energy substitutes, with hydrogen developing as a promising candidate because of its high energy capacity, sustainability, and zero CO_2 emissions.[5] When related to hydrogen production approaches, water electrolysis stands out as a carbon-free approach.[6] This process comprises the anodic Oxygen Evolution Reaction and the cathodic Hydrogen Evolution Reaction, where OER is kinetically sluggish due to a four-electron transfer.[7] Precious metals such as IrO_2 and RuO_2 for OER, Pt/C for HER, are considered state-of-the-art catalysts and face limitations due to scarcity and cost.[8,9] Hence, low-cost and earth-abundant electrocatalysts are required for mass hydrogen production. Transition metal-based catalysts, such as carbides,[10] nitrides,[11–13] and hydroxides,[14–16] shown promise for OER. Layered double hydroxides (LDHs) such as CoNi-LDH and NiV-LDH exhibit improved OER activity in alkaline media, but it is not efficient for HER due to low conductivity and poor active sites, which led to difficulties in performing both OER and HER in the same electrolyte.[17–21]

Researchers have recently developed a range of approaches to address these challenges, such as incorporating cations, performing anion exchange, combining materials with conductive substrates, formation of heterostructures, and introducing vacancies.[7,22,23] Among these, designing a heterogeneous heterojunction is considered an effective strategy comprising multiple constituents to regulate electron redistribution.[24] Integrating hierarchical structures with increased surface area provides numerous active sites essential for the HER and the OER processes.[25,26] Lee et.al., prepared a novel hollow nanotriangle of NiFe-LDH-$CoMoS_x$, which facilitates the interfacial charge transfer and improves the bifunctional electrocatalytic activity.[27] Wang et al., developed a $FeNi_2S_4$/NiFe-LDH heterostructure interface, which shows improved water-splitting efficiency. This enhancement was primarily attributed to the charge redistribution resulting from the formation of the heterojunction.[28] Similarly, Yang et.al. designed the MoS_2/NiCo-LDH heterostructure as a p-n heterojunction, which shows the synergistic interaction between NiCo-LDH and MoS_2, which act as OH^- and H acceptors, respectively, which leads to improved total water splitting.[29] Also, Yun et al. created a hierarchical CoNiP/NiFe-LDH heterostructure, which showed pronounced activity and prolonged stability due to a synergistic interaction between CoNiP and NiFe-LDH.[30] Moreover, several studies have focused on electron transfer in the heterogeneous LDH interface such as metal oxide/LDH, metal/LDH, and carbon material/LDH. However, there are very few studies on electron redistribution in two heterogeneous LDH interfaces. Hence, it is necessary to design a novel electrocatalyst heterostructure that enhances the charge transfer between two LDH materials. Recently, Rong et al., synthesized a CoFe-LDH/NiFe-LDH heterostructure that exhibits an improved electrocatalytic performance for both HER and OER in an alkaline medium.[31] Owing to the strong binding affinity of hydroxide anion toward the LDH layer which favors water dissociation with the 2D nanosheets of large specific surface area. Hence, we developed a hierarchal NiFe-LDH/NiCo-LDH over Ni foam by two-step

View Article Online
DOI: 10.1039/D5TA04519C

hydrothermal method is expected to yield an efficient electrocatalyst where coupled LDH leads to enhancement in the activity of NiFe-LDH/NiCo-LDH/Ni under an alkaline medium. When compared to NiFe-LDH and NiCo-LDH, NiFe-LDH/NiCo-LDH/Ni shows OER activity with a minimum overpotential of 233 mV (current density-50 mA cm^{-2}) and a further it lower Tafel slope value of 40 mV dec^{-1}. In the case of HER, NiFe-LDH/NiCo-LDH/Ni requires an overpotential of 114 mV to reach a current density of 50 mA cm^{-2} and with a Tafel slope value of 104 mV dec^{-1}. Besides, the electrocatalyst was subjected to the chronoamperometric test, it exhibits prolonged stability of 60 h at applied potentials of about 1.55 V vs RHE in alkaline conditions, respectively. The improvement in OER activity was further confirmed via Bode analysis at various potentials. The lower resistance and higher conductivity of NiFe-LDH/NiCo-LDH reveal the enhanced reaction kinetics. The catalyst's selectivity was verified via faradaic efficiency (FE) measurement by the rotating ring disc electrode (RRDE) technique. NiFe-LDH/NiCo-LDH reveals a higher FE of 93.4%. Turnover Frequency (TOF) was verified for the NiFe-LDH/NiCo-LDH showing a higher TOF value of 0.155 sec^{-1} which is 13 and 24 times superior to that of NiFe-LDH (0.0125 sec^{-1}) and NiCo-LDH (0.0063 sec^{-1}), respectively. The pH-dependent study was performed for NiFe-LDH/NiCo-LDH heterostructure at various pH which reveals the heterostructure follows adsorbate enhancement mechanism (AEM) rather than the lattice oxygen mechanism (LOM). DFT studies for OER process revealed that the formation of M-OOH is the rate-determining step, shows the reduced ΔG_3 value of 1.64 eV (NiFe-LDH/NiCo-LDH) as compared to that of 1.74 eV (NiCo-LDH). Moreover, a reduction in ΔG_H^* enhances both H desorption and adsorption processes, therefore boosting the HER efficiency. Overall, the boosted electrocatalytic activity of NiFe-LDH/NiCo-LDH, as proved by DFT simulations, highlights its importance for efficient water-splitting reactions.

View Article Online
DOI: 10.1039/D5TA04519C

Experimental section

Synthetic route of NiCo-LDH/NF, NiFe-LDH/NF and NiFe-LDH/NiCo-LDH/NF:

Commercial NF was made into 4×0.5 cm^2 pieces and rinsed with 1 M dilute HCl, acetone, and ethanol with deionized water for almost 30 min. Then, NiCo-LDH and NiFe-LDH were made separately on Ni foam through the hydrothermal method. NiCo-LDH was synthesized based on the previous literature report.[18] At first 0.357 g (1.5 mmol) of $Ni(NO_3)_2.6H_2O$, 0.175 g (0.7 mmol) of $Co(NO_3)_2.6H_2O$, and 0.6 g (10 mmol) of urea and 0.074 g (0.03 mmol) of NH_4F were dissolved in 40 mL of deionized water and the solution was undergone to ultrasonic dispersion for 10 min to attain a uniform solution. Then the entire mixture was shifted into 50 mL Teflon-lined stainless steel and subjected to heating at 180 °C (12 h). Then similar procedure has to be adopted for the synthesis of NiFe-LDH over Ni foam (NF), where 0.357 g (1.5 mmol) of $NiCl_2.6H_2O$, 0.175 g (0.7 mmol) of $FeCl_3.6H_2O$ and 0.6 g (10 mmol) of urea and 0.074 g (0.03 mmol) of NH_4F were dissolved in 40 mL of deionized water and the mixture was subjected to hydrothermal process.[32] The NiFe-LDH/NiCo-LDH/NF was made by second hydrothermal reaction over NiCo-LDH/NF, where 0.357 g of $NiCl_2.6H_2O$ (1.5 mmol), 0.175 g of $FeCl_3.6H_2O$ (0.7 mmol), 0.6 g of Urea (10 mmol) and NH_4F (0.8 mmol) was dissolved in 40 ml of distilled water for subjected to hydrothermal condition at 160 °C for 12 h. The detailed synthesis process is depicted in **Scheme 1.**

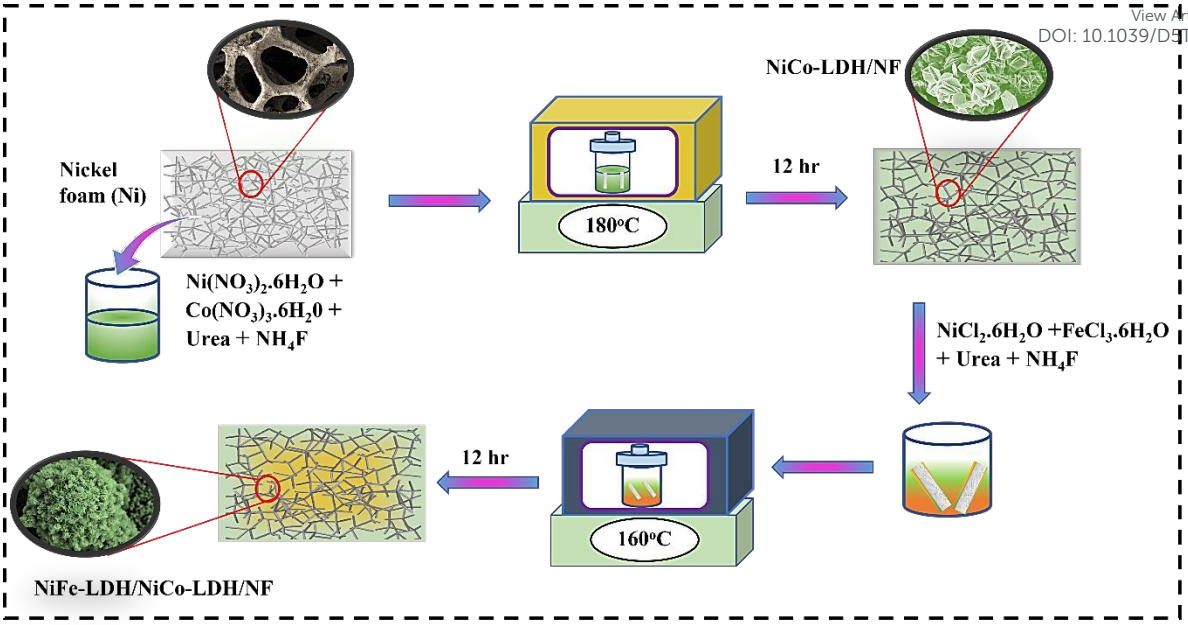

Scheme 1: Schematic illustration of the synthesis of NiFe-LDH/NiCo-LDH/NF.

Results and Discussions

The NiFe-LDH/NiCo-LDH were yielded in an aqueous solution for a two-step hydrothermal reaction. The obtained sample of NiFe-LDH/NiCo-LDH was subjected to ultrasonic treatment for X-ray diffraction (XRD) characterisation, and hence it was peeled off from the foam. The XRD patterns of NiFe-LDH, NiCo-LDH, and NiFe-LDH/NiCo-LDH are shown in **Figure 1a**. The peaks obtained at 11.85, 23.63, 34.54, 35.58, and 46.97° correspond to (003), (006), (009), (015) and (018) planes of NiCo-LDH (JCPDS-033-0429) and the peak at 19.10° corresponds to (001) plane of the β-phase of NiCo-LDH.[33] On the other hand, the peaks at 10.19, 20.42, 22.41, 31.28, and 54.45° correspond to (003), (006), (009), (015) and (018) planes, respectively, revealing the formation of NiFe-LDH (JCPDS-040-0215). Similarly, the peaks observed for NiFe-LDH/NiCo-LDH at 11.36, 22.83, 33.24 and 38.68° corresponds to (003), (006), (015) and (018) planes respectively and the plane (003) and (006) are shifted towards higher 2θ values which indicate lattice contraction in the LDHs layer and confirming the successful growth of NiFe-LDH over NiCo-LDH/NF. The obtained diffraction pattern of NiFe-LDH over NiCo-LDH/NF reveals the polycrystalline nature of the heterostructure.

View Article Online
DOI: 10.1039/D5TA04519C

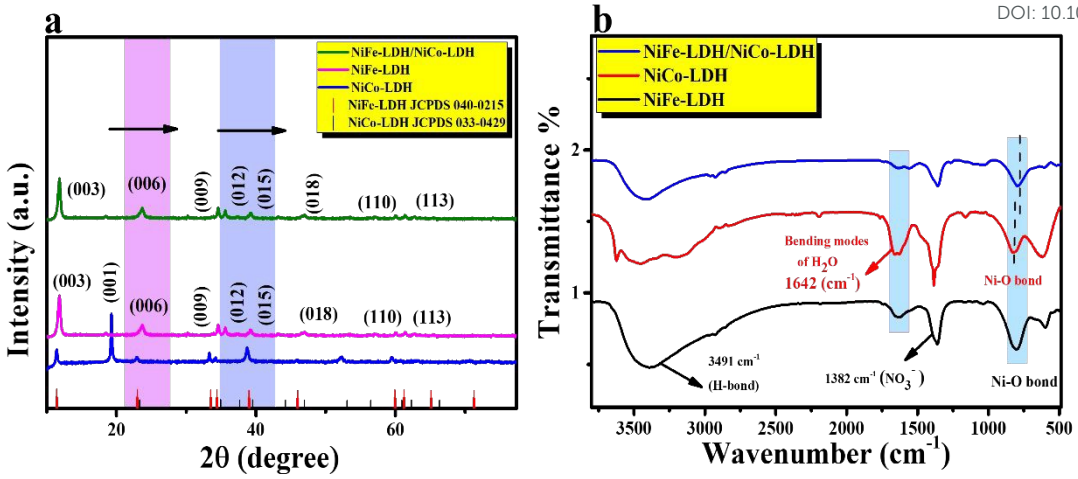

Figure 1: (a) XRD pattern for NiCo-LDH, NiFe-LDH and NiFe-LDH/NiCo-LDH, (b) IR spectra for NiCo-LDH, NiFe-LDH and NiFe-LDH/NiCo-LDH respectively.

To analyze the functional group that exists in the NiFe-LDH/NiCo-LDH, the Fourier transform Infra-Red Spectroscopy (FT-IR) technique was performed. **Figure 1b** represents the corresponding FT-IR spectra for powder samples of NiFe-LDH, NiCo-LDH and NiFe-LDH/NiCo-LDH. A strong absorption band at 3491 and 3480 cm^{-1} corresponds to hydrogen bonding of -OH molecule in NiCo-LDH and NiFe-LDH, respectively.[17] The peak intensity of the -OH group in NiFe-LDH/NiCo-LDH is decreased as compared to NiCo-LDH and NiFe-LDH, suggesting that NiFe-LDH was formed over the NiCo-LDH layer. The peak at 1642 cm^{-1} is observed in the two LDH materials, representing the bending mode of vibration in H_2O molecules. The presence of nitrate ions in the interlayer LDH is confirmed by the related peak at 1382 cm^{-1} show the stretching vibration of NO_3^- anion. The vibrational bands observed at 500-700 cm^{-1} correspond to oxide-metal-oxide (O-M-O), metal-oxide (M-O) and metal-oxide-metal (M-O-M) bonds (M=Fe/Ni).[18,32] The generation of heterojunction between NiFe-LDH and NiCo-LDH with the change in functional properties was confirmed by the decrease in the intensity of M-O bond in NiFe-LDH/NiCo-LDH.

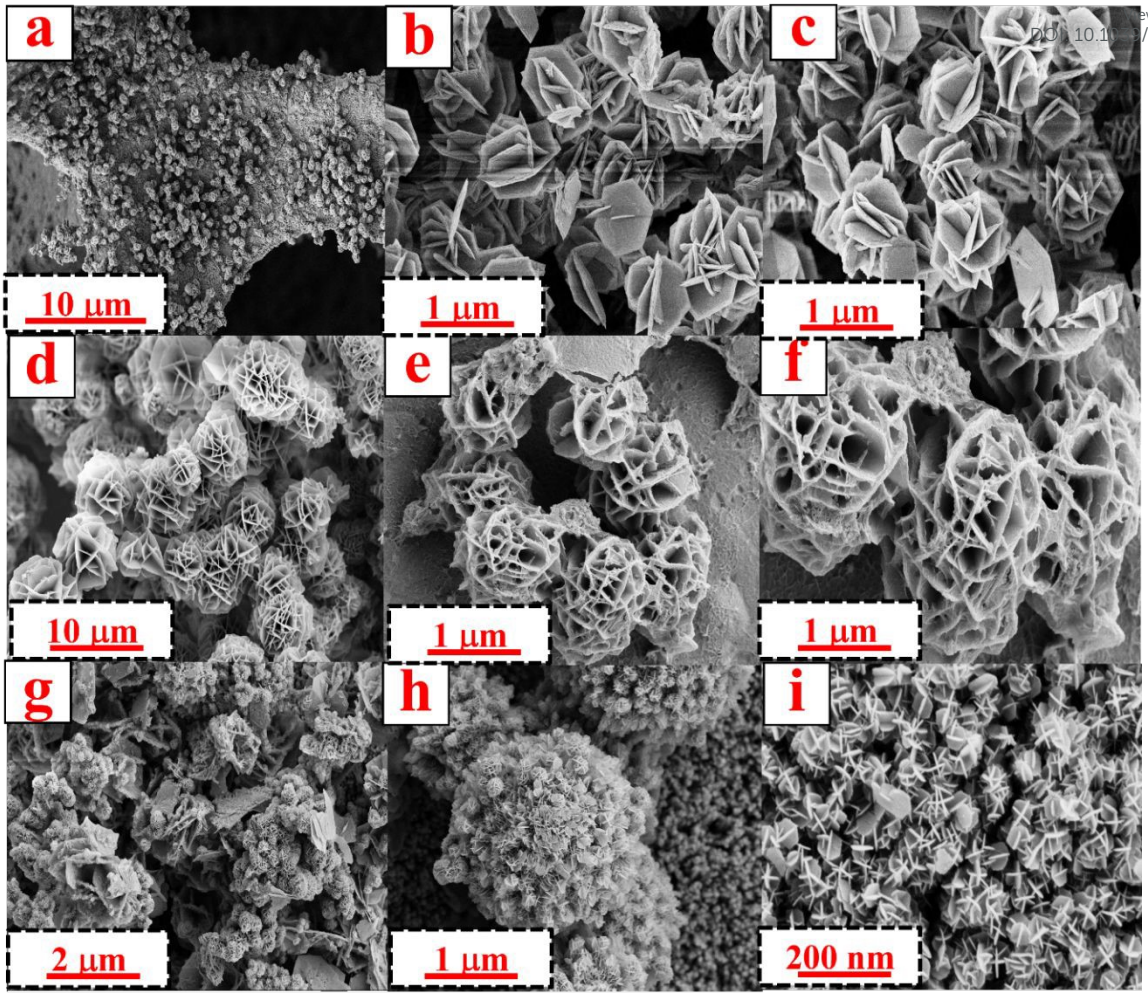

Figure 2: (a-c) The low to high magnification FE-SEM images of NiCo-LDH/NF; (d-f) NiFe-LDH/NF and (g-i) NiFe-LDH/NiCo-LDH/NF respectively.

The morphological details of NiCo-LDH, NiFe-LDH, and NiFe-LDH/NiCo-LDH were confirmed by field emission scanning electron microscopy FESEM analysis. The FESEM images in **Figures 2(a-c)** and **2(d-f)** show the 3D microflower structure of NiCo-LDH and NiFe-LDH, respectively, decorated over Ni foam, in which ultrathin nano petals improve mass transport and ion transport of electrolyte.[34,35] The 3D network of Ni foam offers a site for the formation of LDH materials and results in the creation of an interface between the LDHs and Ni foam. The NiFe-LDH/NiCo-LDH micro-flower has adjacent nano-petals with mesoporous sites which offer channel for conducting the electroactive species (**Figure 2(g-i)**). This unique morphology delivers enhanced OER and HER electrocatalytic performance in the

View Article Online
DOI: 10.1039/D5TA04519C

heterostructure NiFe-LDH/NiCo-LDH/Ni. Inductively Coupled Plasma Mass Spectrometry (ICP-MS) analysis for conducted for the LDH materials to calculate the elemental concentrations of Ni, Co, and Fe. The measured concentrations (in ppm), along with the corresponding atomic ratios for NiCo-LDH/NF, NiFe-LDH/NF, and NiFe-LDH/NiCo-LDH/NF, are Ni: Co (1.92:1), Ni: Fe (1.81:1), and Ni: Co: Fe (1.66:0.37:1), respectively are presented in **Table S2.** To further confirm the morphological aspect of NiCo-LDH, NiFe-LDH and NiFe-LDH/NiCo-LDH were also analyzed by a High-Resolution Transmission electron microscope (HR-TEM). **Figure 3(a-b)** shows a lower to higher magnification image, revealing the nanoflower morphology of NiCo-LDH grown over the nickel foam. From the **Figure 3c**, displays the lattice fringes with a d spacing value of 0.36 nm which corresponds to (006) plane and **Figure 3d** shows the selected area electron diffraction pattern, where the plane (110) corresponds to an interplanar distance of 0.15 nm confirming the polycrystalline nature of NiCo-LDH. Similarly, in **Figure 3(e-f)** shows the nanoflower-like morphology of NiFe -LDH, while the lattice fringes in **Figure 3g** indicate the d spacing value of 0.26 nm which corresponds to (012) plane. The SAED pattern of NiFe-LDH in **Figure 3h** shows d spacing value of 0.151 nm (red circle) and 0.230 nm (yellow circle) which related to (113) and (015) respectively, further confirming its polycrystalline nature. Moreover, the HRTEM images of NiFe-LDH/NiCo-LDH in **Figure 3(i-j)** clearly show the vertically aligned NiFe-LDH sheets over the NiCo-LDH sheet, confirming the formation of heterostructure between the NiFe-LDH and NiCo-LDH. From **Figure 3k** reveals the HR-TEM images of distinct lattice fringes with interplanar spacings of 0.26 and 0.36 nm, attributed to the (012) and (006) planes of NiFe-LDH and NiCo-LDH respectively. On the other hand, the SAED pattern in **Figure 3l** reveals the interplanar spacings of 0.15 nm for the (113) planes of NiCo-LDH and 0.26 nm for the (012) planes of NiFe-LDH which matches with XRD pattern of NiFe-LDH/NiCo-LDH material. **Figure 3m,** represents the existence of all the elements was analysed using High angular angle

Dark Field imaging (HAADF imaging) and confirms the uniform distribution of all expected element such as Ni, Fe, Co and O elements as represented in **Figure 3(n-q)** respectively. These results confirm the successful formation of heterostructure between NiCo-LDH and NiFe-LDH. Further, the presence of Ni, Fe, O, and Co in NiFe-LDH/NiCo-LDH was proved by the EDS spectrum obtained in HRTEM **(Figure (S1).**

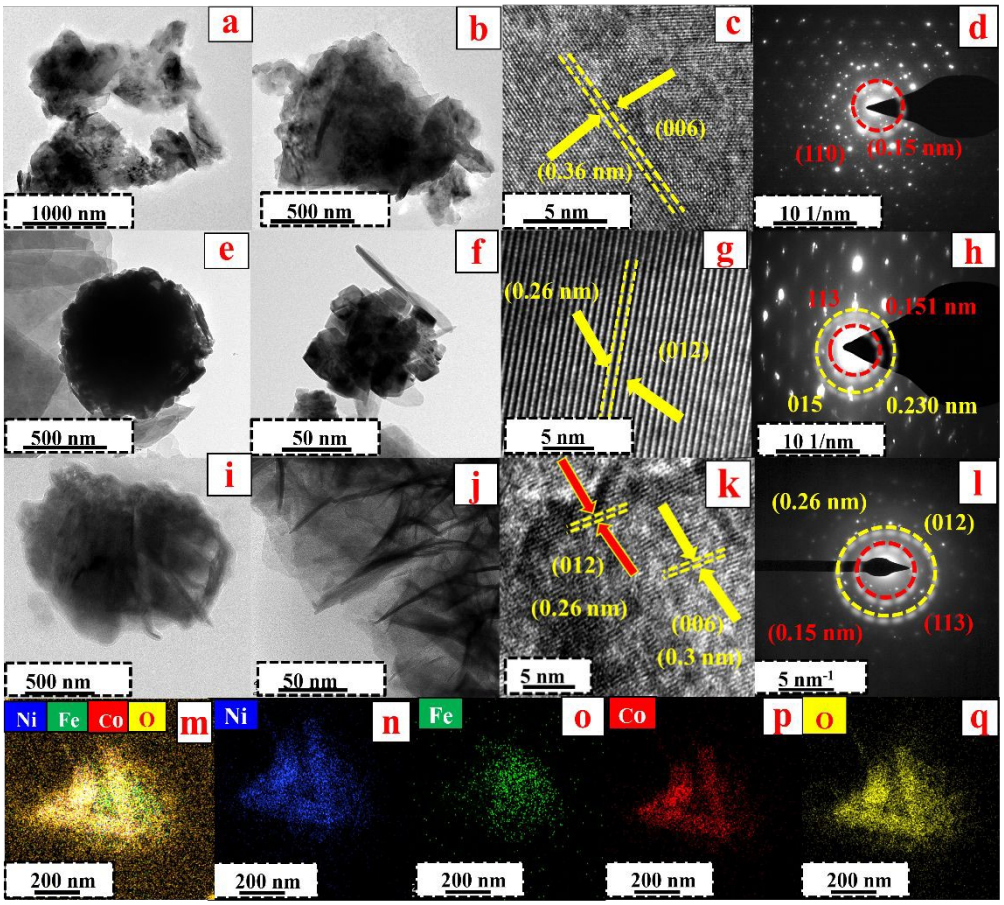

Figure 3: (a-b) The low to high magnification HRTEM images of NiCoLDH/NF; (c) lattice fringes; (d) SAED pattern for NiCo-LDH/NF. (e-f) the low to high magnification HRTEM images of NiFe-LDH/NF; (g) lattice fringes; (h) SAED pattern for NiFe-LDH/NF. (i-j) the low to high magnification HRTEM images; (k) lattice fringes; (l) SAED pattern for NiFe-LDH/NiCo-LDH/NF; (m) HAADF imaging and (n-q) color mapping shows uniform distribution of Ni, Fe, Co and O respectively.

The specific surface area of NiCo-LDH, NiFe-LDH and NiFe-LDH/NiCo-LDH electrocatalyst was determined by using Brunauer-Emmett-Teller (BET) analysis which indicates the nitrogen

View Article Online
DOI: 10.1039/D5TA04519C

adsorption-desorption isotherms.[36] As shown in **Figure S2a**, all the material exhibits Type II isotherms, which indicates the characteristic of mesoporous materials with a steady increase in gas adsorption with increasing relative pressure. The NiFe-LDH/NiCo-LDH heterostructure exhibits a significantly larger specific surface area (70.89 m²/g) compared to bare NiCo-LDH (15.01 m²/g) and NiFe-LDH (28.15 m²/g), respectively (**Figure S2a**). These studies deliver a direct relation between the increased specific surface area of the NiFe-LDH/NiCo-LDH from the wider region of P/P_o between 0.1 to 0.9. Consequently, this larger surface area delivers more active sites for water adsorption and leads to improved water oxidation activity. Barrett-Joyner-Halenda (BJH) Pore size distribution analysis revealed a less intense bimodal pore size distribution (dV/dD) around 3-4 and 4-5 nm for NiCo-LDH (**Figure S2b**), whereas for NiFe-LDH also showed around 4-5 and 6-8 nm (**Figure S2c**). But the Pore size distribution for NiFe-LDH/NiCo-LDH hetero structure possesses more intense trimodal pore size distribution around 4-6, 6-7, and 8-9 nm (**Figure S1d**). This suggests that the growth of NiFe-LDH onto the NiCo-LDH may have introduced new pore structures or slightly expanded existing ones, which delivers the greater availability for ion movement and possesses the increased specific surface area. Therefore, the material with a different range of mesopores and a large specific surface area plays a main role in electrochemical properties. Hence, NiFe-LDH/NiCo-LDH heterostructure is recognized for its superior performance in oxygen evolution reaction (OER).

X-ray photoelectron spectroscopy (XPS) was carried out to examine the prepared samples' oxidation state and chemical composition.[37,38] The Ni 2p XPS spectrum for NiFe-LDH/NiCo-LDH (**Figure 4a**) shows binding energy peaks at 854.1 eV (Ni $2p_{3/2}$) and 873.4 eV (Ni $2p_{1/2}$) respectively. Moreover, a peak at 855.8 eV is attributed to the Ni^{3+} $2p_{3/2}$ state which exhibits a negative shift of 0.54 eV and 0.4 eV compared to bare NiCo-LDH and NiFe-LDH respectively.[39] The XPS spectra for Fe 2p exhibit peaks at 714.9 eV (Fe $2p_{3/2}$) and 722.69 eV (Fe $2p_{1/2}$), showing that Fe exists in the +3 state. Notably, the Fe $2p_{3/2}$ peak in NiFe-LDH/NiCo-

View Article Online
DOI: 10.1039/D5TA04519C

LDH shifted positively by 0.5 eV relative to NiFe-LDH, implying the electrons transfer from NiFe-LDH to NiCo-LDH through an interface heterostructure (**Figure 4b**).

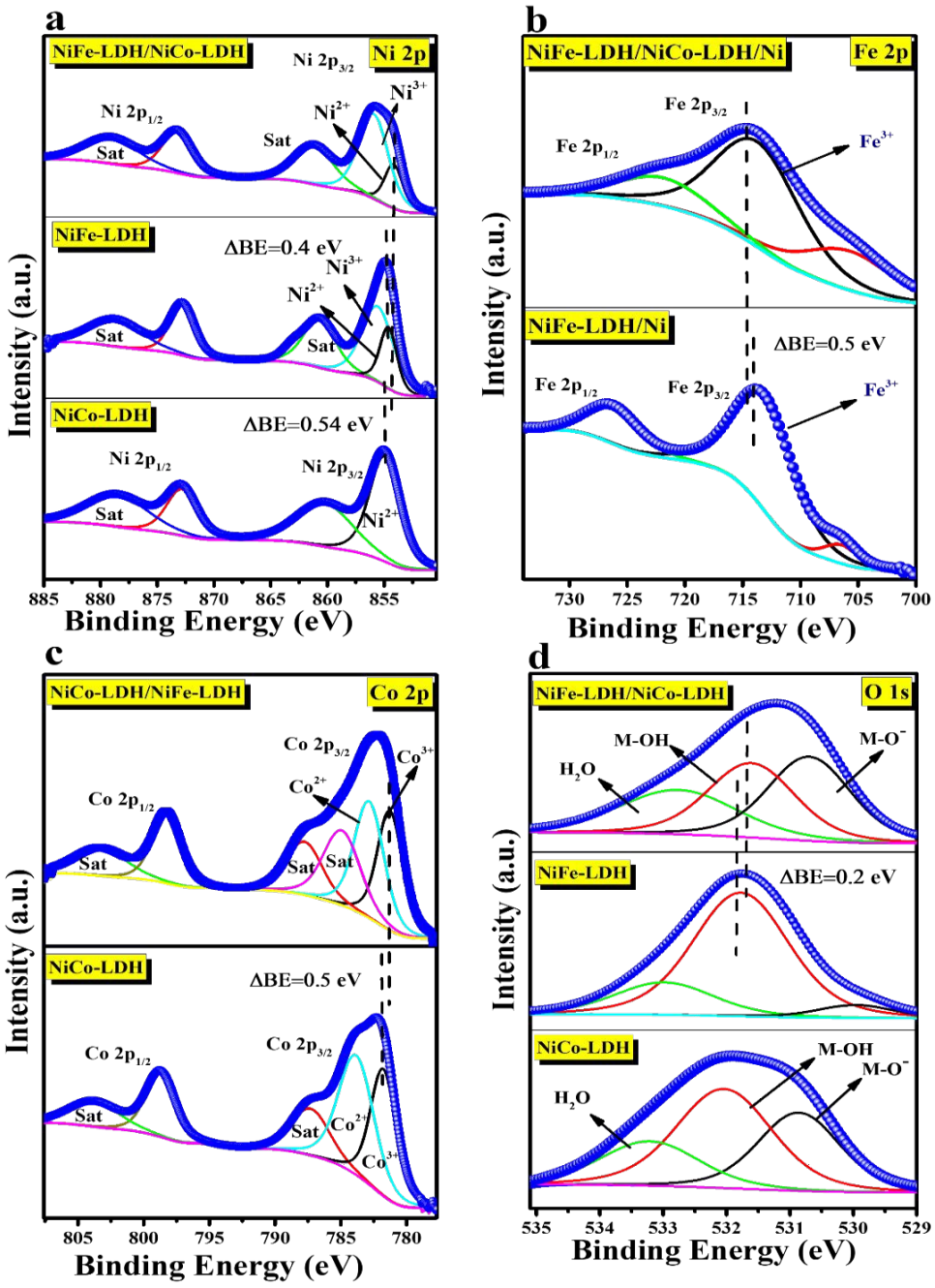

Figure 4 (a-d): The deconvoluted XPS spectra for Ni, Fe, Co and O of NiCo-LDH, NiFe-LDH and NiFe-LDH/NiCo-LDH respectively.

The two binding energy peaks at 781.31 (Co $2p_{3/2}$) and 798.21 (Co $2p_{1/2}$) which indicates the Co exists in the +3 oxidation state.[40] The main peak corresponds to Co^{3+} $2p_{3/2}$ in NiFe-

View Article Online
DOI: 10.1039/D5TA04519C

LDH/NiCo-LDH, indicating a negative shift of 0.5 eV as related to bare NiFe-LDH (**Figure 4c**). The increased peak intensity of Ni^{3+} $2p_{3/2}$ in the NiFe-LDH/NiCo-LDH heterostructure specifies a change in the electronic environment and the intensity ratio of Ni^{3+}/Ni^{2+} increases from 1.01 to 1.02. Also, the intensity ratio of Co^{3+}/Co^{2+} increases from 0.98 to 0.99. The shift toward lower binding energy values with the enhanced Ni^{3+}/Ni^{2+} intensity ratio suggests the strong electronic interaction between the NiCo-LDH and NiFe-LDH. This improved interaction further enhances charge transfer ability, leading to superior electrocatalytic activity. The deconvoluted XPS spectra of O1s for NiFe-LDH/NiCo-LDH display three peaks for oxygen at 531.6, 532.9, and 530.76 eV, which correspond to hydroxyl group (M-OH), oxygen in absorbed water (H_2O), and metal-oxygen (M-O), respectively (**Figure 4d**).[41] The peak corresponds to M-O in NiFe-LDH/NiCo-LDH, exhibiting a negative shift of 0.2 eV when compared to bare NiFe-LDH. The observed shifts in binding energy further prove that an electron is transferred from NiFe-LDH to NiCo-LDH and lead to strong electronic interaction in the heterojunction.

Electrocatalytic OER studies of NiCo-LDH, NiFe-LDH and NiFe-LDH/NiCo-LDH/NF in Alkaline medium:

To investigate the electrocatalytic OER activity for NiFe-LDH/NiCo-LDH/NF heterostructure in 1 M KOH, a conventional three-electrode configuration was used where a Pt and Hg/HgO (1 M KOH) electrode was the counter and reference electrode, respectively.[42] The OER performance of NiFe-LDH/NiCo-LDH/NF heterostructure has been compared with bare NiCo-LDH, NiFe-LDH via the LSV polarization studies at the scan rate of 5 mV/s in alkaline 1M KOH solution. The bare NiCo-LDH, NiFe-LDH, RuO_2 and NF exhibit a higher overpotential value of 310, 270 mV, 330 mV and 390 mV, respectively at 50 mA/cm^2 (**Figure 5a**), whereas NiFe-LDH/NiCo-LDH/NF exhibits impressive performance, showing the overpotential of 233 mV at a similar current density. The observed Tafel slope value for NiFe-

LDH/NiCo-LDH/NF is 40 mV/dec, which is noticeably lower than that of bare NiCo-LDH (60 mV/dec), NiFe-LDH (52 mV/dec), RuO_2 (126 mV/dec) and Nickel Foam (185 mV/dec) (**Figure 5b)**. This Tafel slope signifies that the NiFe-LDH/NiCo-LDH/NF shows faster electron transfer kinetics as compared to other catalysts. The electrochemical impedance spectroscopy (EIS) was executed to estimate the charge transfer resistance (R_{ct}) for all the catalysts (**Figure 5c)**. The NiFe-LDH/NiCo-LDH/NF heterostructure delivered a lower R_{ct} value of 0.836 Ω, whereas the bare NiCo-LDH, NiFe-LDH, RuO_2, and NF have R_{ct} values of 2.45 Ω, 2.88 Ω, 3.51, and 6.21 re,spectively, which reveals the lower resistivity toward the electrode-electrolyte interface. Additionally, LDH material possesses ultra-thin nano petals having macro-void channels, which enhance the mass and charge transfer at the electrode/electrolyte interface. Also, the turnover frequency (TOF) was evaluated at 1.49 V and the values are 0.0063, 0.012 and 0.155 s^{-1} for NiCo-LDH/NF, NiFe-LDH/NF and NiFe-LDH/NiCo-LDH/NF, respectively and NiFe-LDH/NiCo-LDH/NF possesses higher OER performance as shown bar diagram in **Figure 5d**. To measure the high electrochemical activity of the hierarchical heterostructure material, the electrochemical active surface area (ECSA) analysis was performed through the double layer capacitance (C_{dl}) method by considering CV results with various scan rates (**Figure S3(a-c)**). The observed C_{dl} values of bare NiCo-LDH/NF, NiFe-LDH/NF and NiFe-LDH/NiCo-LDH/NF are measured by depicting the disparity between cathodic and anodic current (ΔJ) against the different scan rate of 30-150 mVs^{-1} (**Figure 5e**). From **Figure 5e**, the C_{dl} of NiFe-LDH/NiCo-LDH/NF was a much higher value of 16.3 $mFcm^{-2}$ than that of NiFe-LDH/Ni (7.7 $mFcm^{-2}$) and NiCo-LDH/NF (5.58 $mFcm^{-2}$). The OER activity was further ensured by the ECSA normalised curve was resultant from LSV polarisation curve, which displays a similar trend in intrinsic activity as represented (**Figure S4).** The calculated ECSA values for bare NiCo-LDH/NF, NiFe-LDH/Ni, and NiFe-LDH/NiCo-LDH/NF are 139.5, 192.5 and 422.5 respectively.

View Article Online
DOI: 10.1039/D5TA04519C

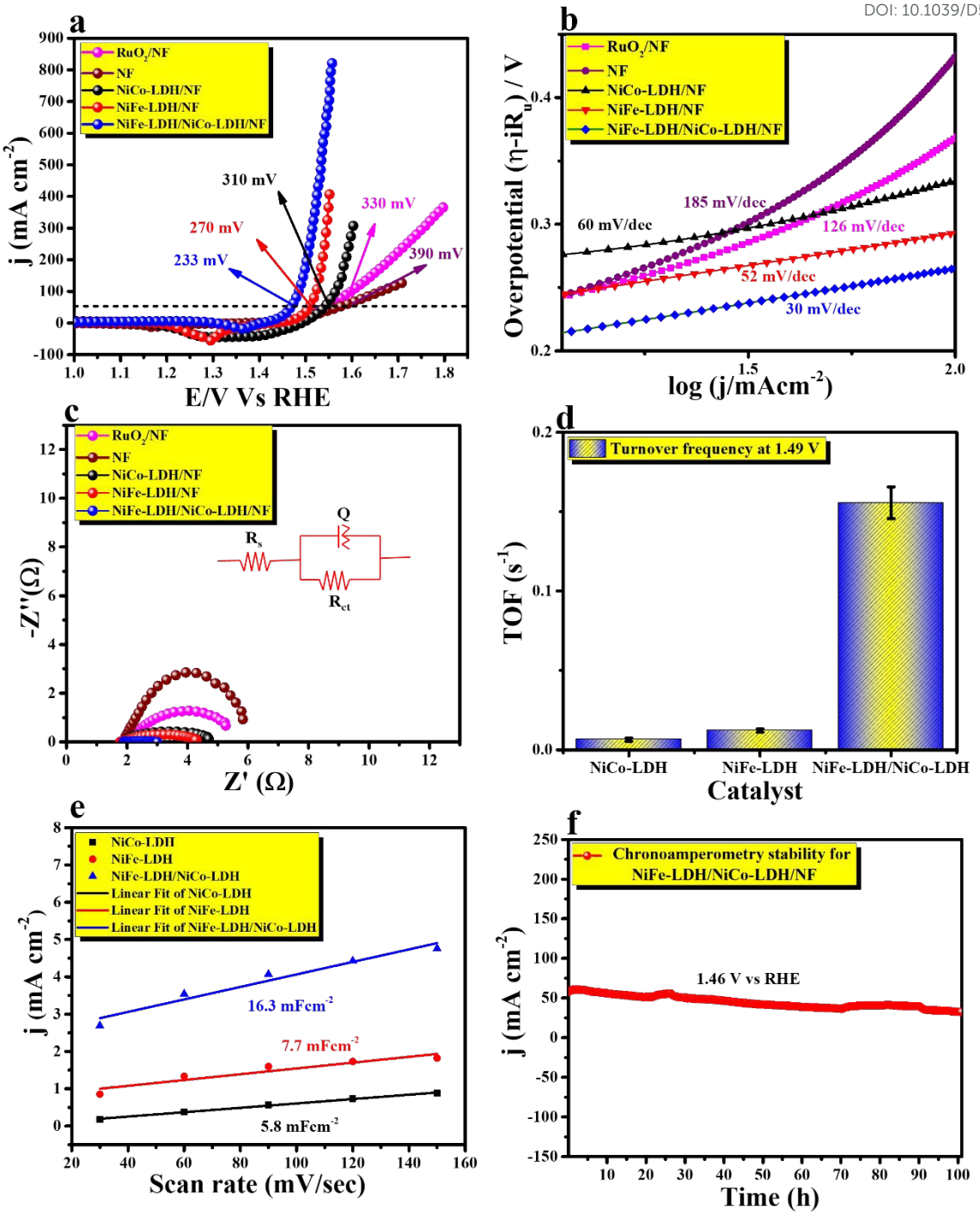

Figure 5: (a) Backward LSV curve at a scan rate of 5 mV/s in 1M KOH for NiCo-LDH, NiFe-LDH, and NiFe-LDH/NiCo-LDH, RuO_2/NF, NF (b) Tafel slope extracted from the LSV polarisation curve (c) Nyquist plot obtained from EIS at 0.80 V (vs Hg/HgO electrode) (d) TOF plot, (e) plot showing the extraction of C_{dl} for calculating ECSA of NiCo-LDH, NiFe-LDH and NiFe-LDH/NiCo-LDH and (f) Long term chronoamperometry study of NiFe-LDH/NiCo-LDH for 100 h in OER 1 M KOH solution.

View Article Online
DOI: 10.1039/D5TA04519C

The high ECSA values for NiFe-LDH/NiCo-LDH/NF indicate a larger exposed surface area for the adsorption of electrolyte ions over the electrode surface. The reduction area was calculated by quantifying the reduction peak area, and observed values are 0.00135, 0.0042, and 0.00659 VA for NiCo-LDH/NF, NiFe-LDH/NF and NiFe-LDH/NiCo-LDH/NF, respectively (**Figure S5(a-c)**). The chronoamperometry (CA) measurement was conducted for NiFe-LDH/NiCo-LDH/NF to evaluate the sustained electrochemical stability delivered for 100 h at 1.46 V versus RHE (**Figure 5f**). After measuring the activity and stability of the NiFe-LDH/NiCo-LDH heterostructure, the selectivity was calculated by measuring Faradaic efficiency. Initially, the collection efficiency (N) was experimentally measured by a rotating ring-disk electrode (RRDE) technique (**Figure S6)**. LSV was performed for the ferro-ferri redox system by using 0.1 M KNO_3 and 10 mM $K_3[Fe(CN)_6]$ at various rpm and the resultant results are summarized in **Table S3,** and the average collection Efficiency (N) value was 0.248. The Rotating Ring Disc Electrode (RRED) was used to quantify the current response during the oxygen evolution reaction. It is highly effective technique for evaluating Faradaic efficiency, which measures the amount of O_2 evolution corresponding to the net charge passed during the electrochemical reaction.[43] The outcomes are depicted **(Figure S7c),** revealing that the disc current of NiFe-LDH/NiCo-LDH catalyst was obtained as 1.27 mA with an applied potential of 1.65 V vs RHE for scan rate (1600 RPM), yielding a Faradaic Efficiency of 93.4%. Notably, the disc current represents the oxygen evolution reaction (OER), while the ring current corresponds to the oxygen reduction reaction (ORR). In contrast, the NiCo-LDH and NiFe-LDH catalysts displayed a disk current of 0.48 and 0.99 mA under identical conditions (**Figure S7a and S7b**), yielding a Faradaic efficiency of 70.85 and 77.7%, respectively. The oxygen bubbles evolved at the disk electrode were efficiently reduced over the Pt ring electrode, which was maintained at a constant potential of -0.23 V. The high Faradaic efficiency reveals the superior selectivity of the NiFe-LDH/NiCo-LDH catalyst for the OER. Further to investigate

View Article Online
DOI: 10.1039/D5TA04519C

the details for enhanced redox activity of NiFe-LDH/NiCo-LDH/NF over bare NiCo-LDH/NF, NiFe-LDH/NF, an operando EIS analysis was performed, which delivers much important information about the adsorption-desorption kinetics of the reactant species over the catalytic interface.[44,45] **Figure S8(a-c)** indicates the corresponding Nyquist plot recorded at various potentials for all three catalysts. Moreover, the Bode plot for each catalyst displays the region where the reactant species adsorbed and desorbed on the catalytic surface, as shown in **Figure S9(a-c)**. The High-frequency region in the Bode plot relates to oxidation/activation of electrode material whereas the Low-frequency region deals with the faradaic OER process. As the potential exceeds 1.22 V *vs* RHE for NiFe-LDH/NiCo-LDH/NF, the phase angle in the High-frequency region starts gradually decreasing, indicating the oxidation of the electrocatalyst. When the potential reaches 1.46 V, the phase angle in the low-frequency region starts to decrease, indicating the OER process has started. However, for NiCo-LDH/NF and NiFe-LDH/NF the OER has started at the potential of 1.53 and 1.50 V, respectively *vs* RHE. From the observed potentials for the OER process, it was clear that NiFe-LDH/NiCo-LDH/NF requires a lower activation region as compared to NiCo-LDH/NF and NiFe-LDH/NF for oxygen evolution. This confirms that NiFe-LDH/NiCo-LDH/NF exhibits lower resistance towards the OER process and shows superior charge transfer kinetics over the electrode/electrolyte interface compared to the other catalysts. The electrochemical study of NiFe-LDH/NiCo-LDH/NF was related to earlier reported catalysts, and the relative outcomes are denoted in **Table S4,** clearly showing that our catalysts accomplish higher OER performance as compared to earlier reported catalysts.

Electrocatalytic HER studies of NiCo-LDH, NiFe-LDH and NiFe-LDH/NiCo-LDH/NF in Alkaline condition:

The electrocatalytic HER study of NiFe-LDH/NiCo-LDH/NF in 1 M KOH solution was tested using LSV at the scan rate of 5 mVs^{-1}. The electrocatalytic activity of three samples such as

NiFe-LDH/NF, NiCo-LDH/NF and NiFe-LDH/NiCo-LDH/NF was tested for comparison. It was observed from **Figure 6a** that the NiFe-LDH/NiCo-LDH/NF shows higher electrocatalytic performance towards HER at 50 $mAcm^{-2}$, requires a minimum overpotential of 114 mV whereas NiFe-LDH/NF, NiCo-LDH/NF, Pt(C) and NF requires 234 mV, 254 mV, 89 mV and 369 mV respectively to reach the similar current density. The increased HER activity of NiFe-LDH/NiCo-LDH/NF could be attributed to hierarchical interfacial engineering, which results in a synergistic effect between NiCo-LDH and NiFe-LDH. To gain a better understanding of HER kinetics, the Tafel slope of all catalyst was calculated using the iR-corrected LSV curve. From **Figure 6b** shows that NiFe-LDH/NiCo-LDH/NF has a lower Tafel slope value (104 mV dec^{-1}) than that of NiFe-LDH/NF (141 mV dec^{-1}), NiCo-LDH/NF (155 mV dec^{-1}) and NF (170 mV dec^{-1}), representing that the combination of NiCo-LDH and NiFe-LDH as a heterostructure is a substantial method to promote the higher HER kinetics. The electrochemical impedance spectroscopy (EIS) was conducted to gain deep insight into the kinetic reaction over the electrode surface represented in **Figure 6c**. The lower charge transfer (R_{ct}) value of 0.416 Ω for NiFe-LDH/NiCo-LDH/NF compares to 0.574, 0.694, and 2.5 Ω for NiFe-LDH/Ni, NiCo-LDH/NF, Pt(C) and NF, respectively. As shown in **Figure 6d**, the chronoamperometric analysis for NiFe-LDH/NiCo-LDH/NF in HER was conducted to investigate long-term electrocatalytic stability at -0.341 V (iR-uncorrected). It is clear that in alkaline conditions, NiFe-LDH/NiCo-LDH/NF exhibits superior HER performance and prolonged electrocatalytic stability for 65 hours. The NiFe- LDH/NiCo-LDH/NF is used as both anode and cathode to analysis the activity for overall water splitting. It was observed from **Figure 6e** that the overall water splitting performance of the catalyst needs a cell voltage of 1.55 V versus RHE to achieve a current density value of 10 mA/cm^2. The chronoamperometric study was performed to analysis the long-term stability of the catalyst NiFe-LDH/NiCo-LDH/NF by providing the constant potential of 1.55 V for 60 hours, has represented in **Figure 6f**.

View Article Online
DOI: 10.1039/D5TA04519C

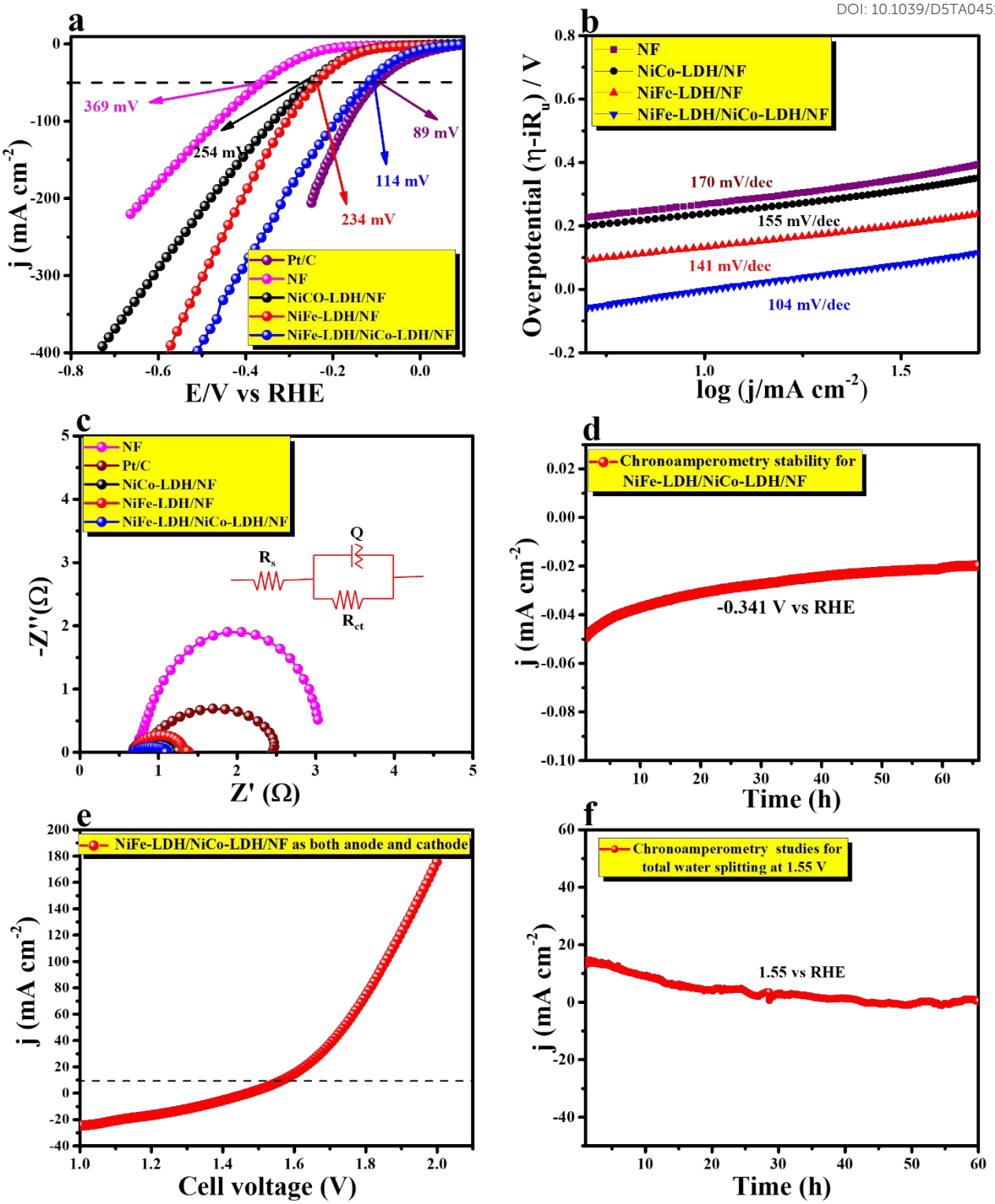

Figure 6: (a) Backward LSV curve at a scan rate of 5 mV/s in 1M KOH for NiCo-LDH, NiFe-LDH, NiFe-LDH/NiCo-LDH, Pt(C) and NF (b) Tafel slope extracted from the LSV polarisation curve (c) Nyquist plot obtained from EIS at 0.80 V (vs Hg/HgO electrode) for the HER (d) Chronoamperometry for NiFe-LDH/NiCo-LDH for 65 h in HER; (e) LSV curve of NiFe-LDH/NiCo-LDH as a cathode and anode in total water splitting; (f) Chronoamperometry for NiFe-LDH/NiCo-LDH based cell to achieve 10 mA/cm^2 for 60 h in total water splitting.

View Article Online
DOI: 10.1039/D5TA04519C

Based on the outcomes from chronoamperometric analysis, it has been noticed that the NiFe-LDH/NiCo-LDH/NF delivers remarkable stability around 46 h without losing any activity. The overall similar results represented in **Tables S5** and **Table S6** show that our catalysts have better HER activity and total water splitting, respectively as compared to the other catalysts.

Post characterisation study of NiFe-LDH/NiCo-LDH

The robustness and morphological features of NiFe-LDH/NiCo-LDH were analyzed after the extended OER application using different characterization methods, such as FESEM, HR-TEM, and XPS. The surface characterisation of the NiFe-LDH/NiCo-LDH/NF catalyst was observed after the prolonged OER stability study through the FESEM technique, as illustrated in **Figure S10(a-c)**. The resulting images demonstrate that the 3D flower-like morphology is sustained even after the prolonged OER stability analysis. **Figure S11(a-b)** shows the HRTEM images of post-treated NiFe-LDH/NiCo-LDH, revealing that the sheet-like morphology remains intact after enduring extreme anodic conditions. In the post NiFe-LDH/NiCo-LDH/NF, the obtained lattice fringes show a d spacing value of 0.3 nm (**Figure S11c**), related to the (012) planes, thereby confirming the formation of nickel oxyhydroxide (NiOOH) intermediate, and it exhibits in polycrystalline illustrated in **Figure S11d**. The High-angle annular dark-field (HAADF) color mapping (**Figure S11e**) confirms the occurrence of Ni, Fe, Co, and O for the post-NiFe-LDH/NiCo-LDH/NF, and the elemental mapping analysis proves the even distribution of these elements after prolonged OER studies (**Figure S11 (f-i)**). Further, the chemical state of the elements in the post-NiFe-LDH/NiCo-LDH was analysed by XPS spectrum. The observed XPS spectra for Ni $2p_{3/2}$ and Ni $2p_{1/2}$ states exhibit peaks at 856.4 and 874.6 eV, respectively, indicating that Ni is in a +3 oxidation state, which is related to NiOOH intermediate (**Figure S12a**). **Figure S12b** shows the binding energy peak at 782.33 eV, which matches the Co $2p_{3/2}$ state, indicating that the Co is in a +3 oxidation state. Similarly, Fe exhibits a characteristics peak at the 782.48 eV (Co $2p_{3/2}$) state, which is related to Fe in the +3 oxidation

View Article Online
DOI: 10.1039/D5TA04519C

state (**Figure S12c**). The observed O1s peak at 531.03, which indicates the metal coordinate oxygen atoms (M-O) bond, Additionally, the peaks appeared at 532.72 and 535.15 eV, which are attributed to M-OH and water molecule (**Figure S12d**). It is worth noting that the O 1s XPS spectra for post-NiFe-LDH/NiCo-LDH show a shift toward a lower binding energy of 0.2 eV after harsh anodic treatment.

Energy band alignment of NiCo-LDH and NiFe-LDH before and after the heterostructure formation

The synergistic charge transfer properties between the NiCo-LDH and NiFe-LDH were studied by using the Mott-Schottky (MS) analysis. From the MS analysis, **Figures 7a and 7b** show that both NiCo-LDH and NiFe-LDH show the negative slope value of -0.77 V and -0.9 V vs RHE, respectively, representing their n-type behavior. From the observed value, NiFe-LDH possesses a high electron density as compared to NiCo-LDH. Consequently, upon the formation of the heterostructure, the effective electron transfer will occur from more n-type NiFe-LDH to less n-type NiCo-LDH, leading to the formation of the strong internal electric field between the valence band and conduction band, which enhances charge separation and transport. This electron transfer from NiFe-LDH to NiCo-LDH continues until the Fermi energy equilibrium is achieved. Due to electron transfer, the formation of a larger number of active sites occurs over the NiFe-LDH, improving the hydroxide ion's adsorption ability and boosting the OER performance. In addition to that band gap of all the catalysts was determined by the Tauc model which establishes the direct relation between the adsorption coefficient (α) and photon energy ($h\nu$) as follows $(\alpha h\nu)^2 = A(h\nu - E_g)$ where $\alpha = 2.303A/L$, L representing the path length of 10 mm, A denoting absorbance of sample. The band gap energy was observed for NiCo-LDH (2.86 eV), NiFe-LDH (1.86 eV) and NiFe-LDH/NiCo-LDH (1.79 eV) by the extrapolation of the intercept of a linear relation of $(\alpha h\nu)^2$ vs. ($h\nu$) to y = 0 as shown in **Figure7(c-e)**.

View Article Online
DOI: 10.1039/D5TA04519C

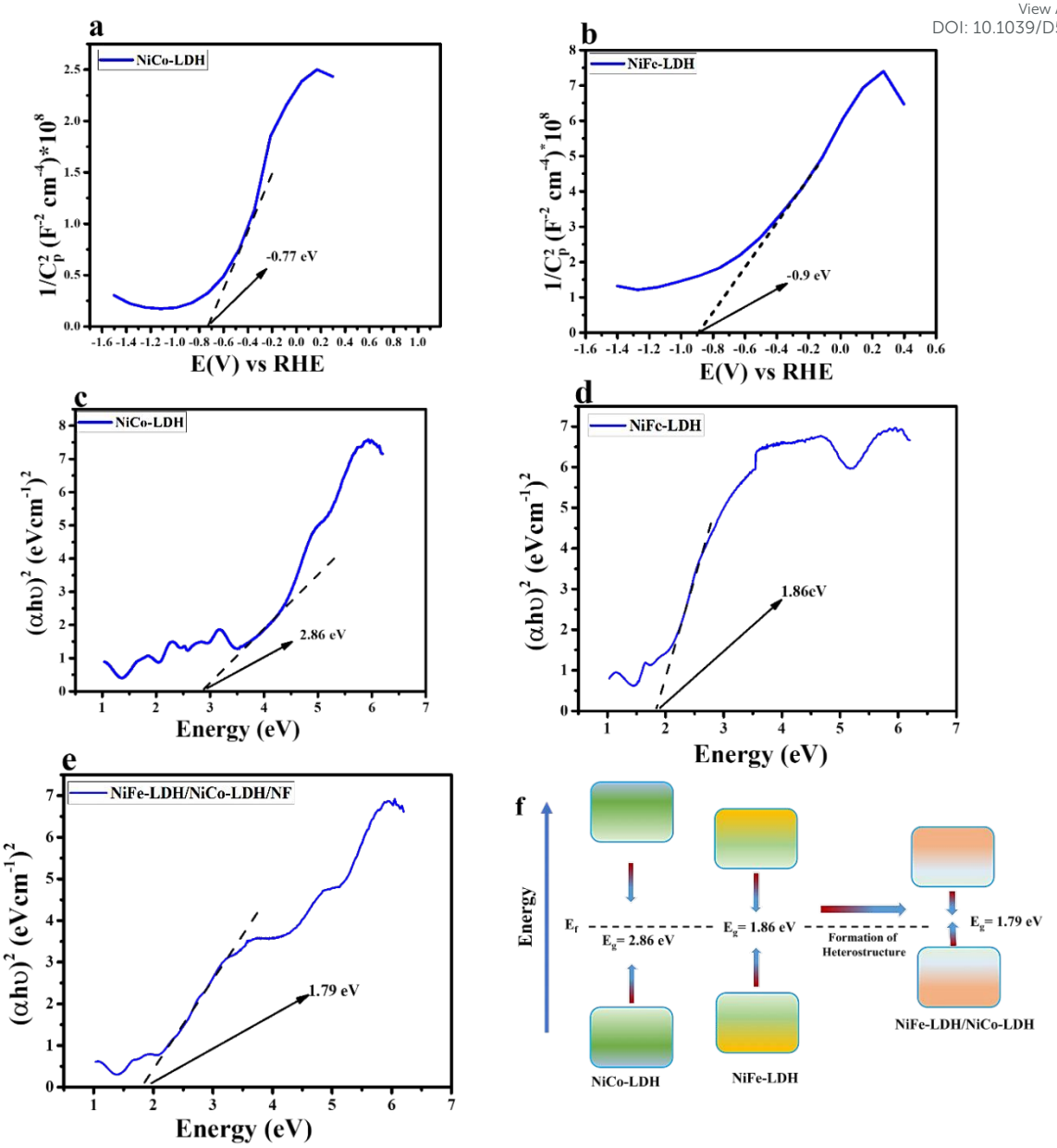

Figure 7: (a-c) Mott-Schottky plots NiCo-LDH, NiFe-LDH (c-e) Tauc plot for NiCo-LDH, NiFe-LDH and NiFe-LDH/NiCo-LDH (f) NiCo-LDH and NiFe-LDH energy band diagram for before and after the formation of heterostructure.

As represented in **Figure 7f**, the effective formation of a n–n heterojunction between NiFe-LDH and NiCo-LDH lowers the bandgap E_g to 1.79 eV. This decrease in bandgap shows enhanced electrical conductivity, as a smaller E_g delivers fast electron transfer from the valence band (VB) to the conduction band (CB).

View Article Online
DOI: 10.1039/D5TA04519C

Electronic interaction:

As earlier discussed, XPS analysis proved the occurrence of strong electronic interaction between NiFe-LDH and NiCo-LDH lattice. Additionally, the Tauc plot confirmed improved electrical conductivity following heterostructure formation. This observation underscores the important role of heterostructure formation in enhancing the OER activity, which could be further verified in terms of electronic interaction and crystal field theory (CFT). In NiFe-LDH and NiCo-LDH, the cations are coordinated by oxygen atoms and reside in an octahedral environment, which will undergo crystal field splitting of d orbitals into t_{2g} and e_g orbitals. Cations such as $Ni^{2+}(\boldsymbol{t_{2g}^6\, e_g^2})$, $Fe^{3+}(\boldsymbol{t_{2g}^3\, e_g^2}$) have symmetrically filled electronic configuration, and hence they do not exhibit Jahn-Teller distortion. However, Ni^{3+} ($\boldsymbol{t_{2g}^6\, e_g^1}$) possesses the unsymmetrically filled electronic configuration and hence Jahn-Teller distortion will occur. Hence, in NiCo-LDH as shown in **Figure S13a**, the partially filled d-orbitals of the Ni^{2+} ion interact with the fully occupied orbitals of the O atom through a weak d_π–p_π interaction, leading to low electronic conductivity. In NiFe-LDH, both Ni^{3+} and Fe^{3+} possess unpaired electrons in d orbitals, which have strong $\boldsymbol{d_\pi}$-$\boldsymbol{p_\pi}$ interaction with the filled p orbital of the O atom as represented in **Figure S13b**. As evident from the XPS spectra (**Figure 4a)** the Ni^{3+} concentration in NiFe-LDH/NiCo-LDH is increased compared to NiFe-LDH, leading to a significant shift in binding energy. This indicates that the electron is transferred from the more n-type NiFe-LDH to the less n-type NiCo-LDH within the heterostructure. Further, in a heterostructure, the filled 2p orbitals of the O atom can easily interact with a vacant d orbital of the Ni^{3+} ion. Moreover, the partially filled d orbitals of Fe^{3+} could easily interact with the filled 2p orbitals of O atom, promoting the synergistic interaction between the Ni^{3+}, $Fe^{3+,}$ and O as illustrated in **Figure S13c**. This reveals the strong electronic interaction between the NiFe-LDH and NiCo-LDH, which is essential for facilitating the fast electron transfer reaction.

Hence, coupling the between the NiFe-LDH and NiCo-LDH into a heterostructure significantly improves electronic conductivity, thereby enhancing both OER and HER performance.

Mechanistic understanding:

The pH-dependent study was demonstrated at under various pH conditions such as 12.5, 13, 13.5, and 14 to verify the reaction mechanism of the NiCo-LDH, NiFe-LDH, and NiFe-LDH/NiCo-LDH electrocatalyst. The OER activities of NiFe-LDH/NiCo-LDH were obtained at various pH conditions represented in **Figure 8a**, for NiCo-LDH and NiFe-LDH are shown in **Figures S14a and S14b**, respectively. The reaction order is an important parameter that offers valuable information about the reaction mechanism in the OER. The reaction order of the LDH material was evaluated at a potential of 1.55V vs RHE. Additionally, a comparative LSV study was conducted using 1 M TMAOH (Tetramethylammonium hydroxide) and 1 M KOH. The TMA^+ cation plays a crucial role in OER activity.[46,47] The OER performance of NiCo-LDH, NiFe-LDH, and NiFe-LDH/NiCo-LDH in 1 M TMAOH electrolytes shows a noticeable decrease in OER activity are represented in **Figure 8b**. This may have the possibility that the LDH electrocatalysts follow the LOM pathway, for NiCo-LDH and NiFe-LDH represented in **Figures S14c and S14d**, respectively. To further confirm this, the reaction orders (ρ =dlogj/dpH) were calculated by the logarithm of current density 'j' as a function of pH and were found to be 0.39, 0.39, and 0.31 on the RHE scale, which corresponds to NiCo-LDH, NiFe-LDH, NiFe-LDH/NiCo-LDH heterostructure, respectively, as illustrated in **Figure 8c**.

View Article Online
DOI: 10.1039/D5TA04519C

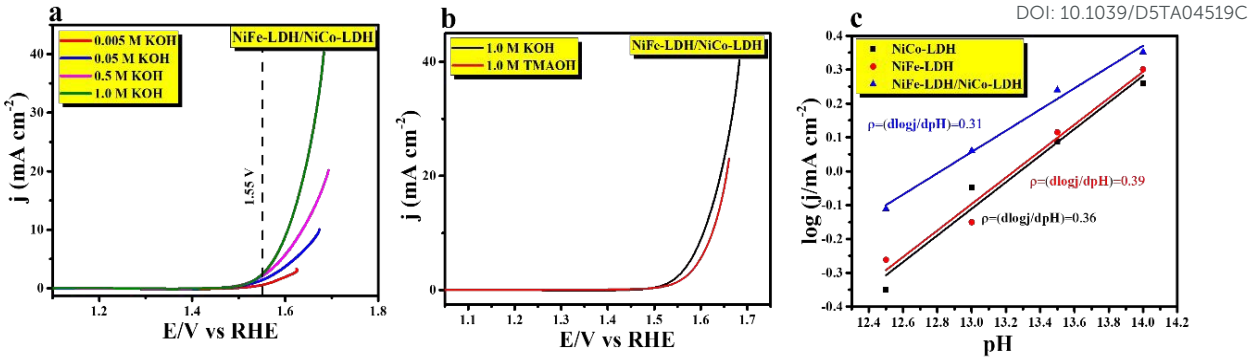

Figure 8: (a) LSV study of NiFe-LDH/NiCo-LDH, at various molar concentrations of 0.005, 0.05, 0.5, and 1.0 M KOH (b) LSV study of NiFe-LDH, NiCo-LDH, and NiFe-LDH/NiCo-LDH in 1.0 M KOH and 1.0 M TMAOH. (c) Reaction order plot.

These values fall within the reaction order of 1, indicating that all LDH materials exhibit weak pH dependence, and thus the reaction mechanism follows the Adsorbate Enhancement Mechanism (AEM) and not the Lattice Oxygen Mechanism (LOM). Raman study was used to relate electrochemical performance with structural changes under operating conditions. Chronoamperometry was carried out for 2 hours at different potentials of 1.42, 1.47, 1.52, and 1.57 V vs. RHE. After the chronoamperometric measurement, the samples were analysed by using quasi-in situ Raman spectroscopy. The spectra revealed three broad peaks cantered at approximately 543, 655, and 1093 cm^{-1}as shown in **Figure 9**. Remarkably, the intensity of those peaks increased gradually with the applied potential, and a slightly shift towards a lower Raman shift was observed. The bands at 543 and 655 cm^{-1} can correspond to $Ni^{(II)}$-O and $Ni^{(III)}$-O in LDH, whereas the peak at 1093 cm^{-1} is characteristic of the Ni-OOH or Co-OOH, which formed as an intermediate in the oxygen evolution reaction (OER) and the peaks increased gradually with the applied potential under anodic polarization.[48,49] These findings, in combination with theoretical studies observed from the **Figure 12a**, strongly support that the Ni or Co sites in the NiCo-LDH regions of the NiFe-LDH/NiCo-LDH heterostructure are the primary active centers for OER.

View Article Online
DOI: 10.1039/D5TA04519C

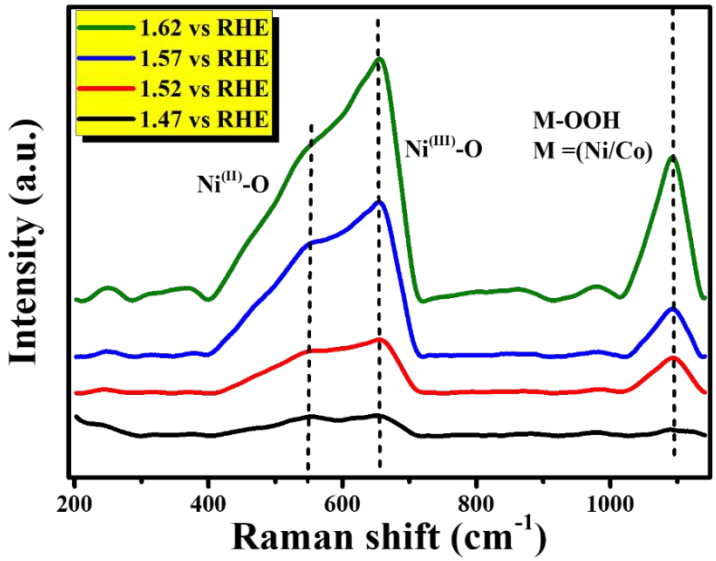

Figure 9: Raman spectra of NiCo-LDH, NiFe_LDH and NiFe-LDH/NiCo-LDH heterostructure, recorded at various potentials 1.47, 1.52, 1.57 and 1.62 vs RHE.

Theoretical Analysis

Crystal Structures of NiFe-LDH, NiCo-LDH and NiFe-LDH/NiCo-LDH heterostructure:

We performed theoretical calculations based on density functional theory (DFT), which focused on modelling a metal-based layered double hydroxide configuration. Our investigation aims to calibrate the Fe and Co content in the NiFe-LDH, NiCo-LDH layer, and in NiCo-LDH@NiFe-LDH heterostructure. We have modelled a 3x2x1 supercell for NiCo-LDH, NiFe-LDH and NiCo-LDH@NiFe-LDH heterostructure with 1:1 molar ratio of Ni: Fe in NiFe-LDH and 2:1 molar ratio of Ni:Co in NiCo-LDH. The optimized configurations for the above proposed configurations are represented in **Figure 10(a-c)**. To gain more insight about the charge transfer mechanism, we have evaluated the charge density difference (CDD) as shown in **Figure 10d.** The charge density difference was derived from $\Delta\rho = \rho_{NiCo\text{-}LDH} - \rho_{NiFe\text{-}LDH}$, where ρ_{NiCo} and ρ_{NiFe} are the electron densities of NiCo-LDH and NiFe-LDH, respectively. The blue region in **Figure 10d** denotes the charge depletion where as the yellow region represents

View Article Online
DOI: 10.1039/D5TA04519C

the charge accumulation have observed a clear charge redistribution due to the NiCo and NiFe layers.

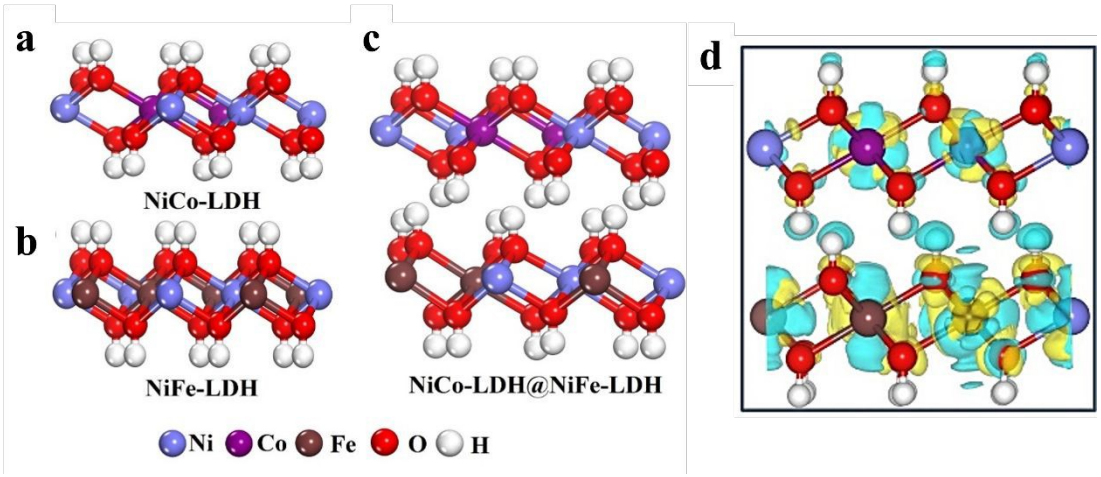

Figure 10: (a-c) Optimized configuration of NiCo-LDH, NiFe-LDH and NiCo-LDH@NiFe-LDH, respectively. Blue, purple, brown, red and white colour balls denote Ni, Co, Fe, O and H atoms respectively. (d) Charge Density Difference (CDD) for NiCo-LDH@NiFe-LDH heterostructure.

The highest charge accumulation is found around NiCo-LDH, and more charge depletion is observed around the NiFe-LDH layer, which represents that NiCo-LDH acts as a charge acceptor and NiFe-LDH acts as a charge donar. This result further corroborates the charge transfer, which shows the 0.1 e^- of charge is transferring from NiFe-LDH to NiCo-LDH.

Electronic Density of States and Charge Transfer Analysis:

To gain more information regarding the electronic structure, we have computed the Density of states (DOS), charge transfer from Bader charges, and charge density difference (CDD) as shown in **Figure 11a,** respectively. The electronic states of the spin-up and spin-down components for the NiCo-LDH, NiFe-LDH and NiCo-LDH@NiFe-LDH heterostructure show anisotropic behavior, representing their magnetic nature. From the density of states, we have observed significant variation in the electronic properties of the heterostructure compared to the single-layer NiCo-LDH and NiFe-LDH. The heterostructure exhibits an intermediate band

View Article Online
DOI: 10.1039/D5TA04519C

gap between NiCo-LDH and NiFe-LDH. The PBE band gaps of the spin-up and spin-down components of NiCo-LDH are found to be 2.12 eV↑ and 2.56 eV↓, respectively. For NiFe-LDH, the band gap values are 1.68 eV↑ and 1.12 eV↓, respectively. In the case of NiCo-LDH@NiFe-LDH heterostructure, the band gaps are reduced to 1.82 eV↑ and 1.18 eV↓, compared to NiCo-LDH.

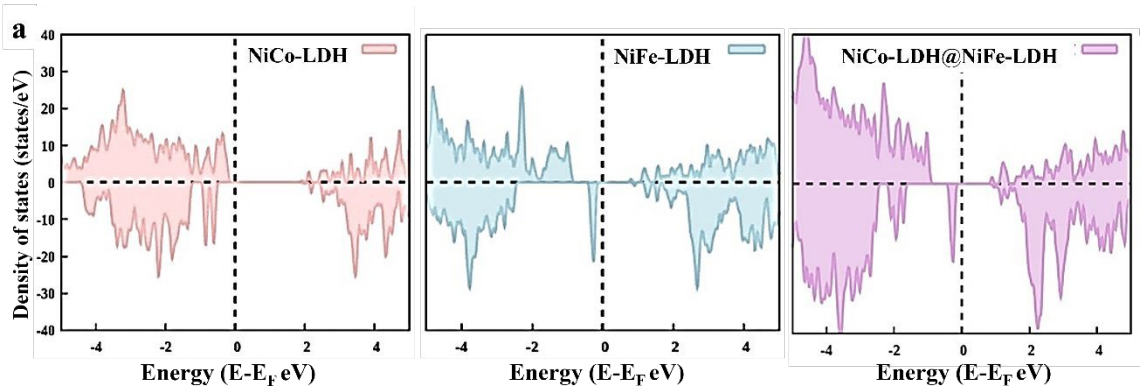

Figure 11: (a) Density of States (DOS) of NiCo-LDH, NiFe-LDH and NiCo-LDH@NiFe-LDH heterostructure, respectively.

The reduction in the band gap for the heterostructure is due to the modification in the electronic structure at the interface because of the electronic interaction between the NiCo-LDH and NiFe-LDH layers. The reduced band gap facilitates better charge transfer in the heterostructure.

The Catalytic Oxygen Evolution Reaction and Hydrogen Evolution Reaction Mechanism:

The DFT calculations were conducted to gain insights into the enhanced oxygen evolution reaction (OER) performance for the NiCo-LDH, NiFe-LDH, and NiFe-LDH@NiCo-LDH heterostructure. In the alkaline conditions, the OER process can be indicated in the following elementary step pathways:

$$OH^- + * \rightarrow *OH + e^- \quad \text{.....(1)}$$

$$*OH + OH^- \rightarrow *O + H_2O\ (g) + e^- \quad \text{.....(2)}$$

View Article Online
DOI: 10.1039/D5TA04519C

$$*O + OH^- \rightarrow *OOH + e^- \text{.....(3)}$$

$$*OOH + OH^- \rightarrow * + O_2(g) + H_2O(g) + e^- \text{ .....(4)}$$

Here, (g), and * denote gas phase, and an active site on the catalyst surface, respectively. While, *OH, *O and *OOH represent adsorbed intermediates.[50] **Figure 12a** depicts the optimized adsorption configurations of the intermediate species and the detailed OER mechanism for the NiCo-LDH@NiFe-LDH heterostructure, highlighting *OH, *O, and *OOH species involved in the reaction.[51]

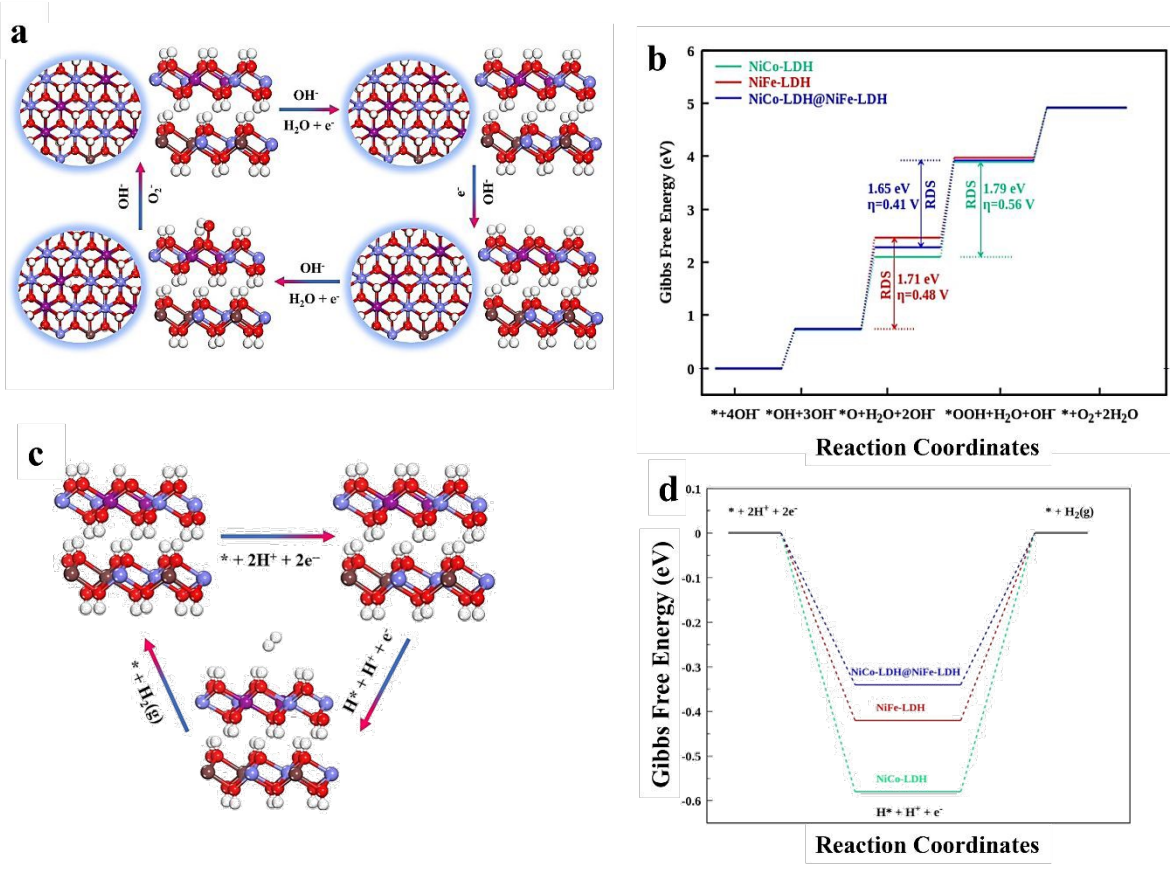

Figure 12: a) Proposed 4e⁻ mechanism of oxygen evolution reaction along with the optimized structures of NiCo-LDH@NiFe-LDH. b) The Gibbs free energy pathways on NiCo-LDH, NiFe-LDH and NiCo-LDH@NiFe-LDH, where the arrows show the rate-determining steps (RDS). c) Proposed mechanism of hydrogen evolution reaction along with the optimized structures of NiCo-LDH@NiFe-LDH. d) The Gibbs free energy pathways on NiCo-LDH, NiFe-LDH and NiCo-LDH@NiFe-LDH.

To evaluate the OER activities of NiCo-LDH, NiFe-LDH and NiCo-LDH@NiFe-LDH heterostructure catalysts, we investigated the free energies of OER intermediates, as depicted in **Figure 12b**. The optimized adsorption configuration and OER mechanism of the single-layer NiFe-LDH and NiCo-LDH are shown in **Figure S15 (a and b).** The thermodynamic overpotential is found to be 0.56 V and 0.48 V for the NiCo-LDH and NiFe-LDH structures, respectively. The overpotential for the heterostructure is significantly reduced to 0.41 V. The OH* protonation to *O is the rate determining step (RDS) with ΔG_2 value of 1.71 eV for the NiFe-LDH, while for the NiCo-LDH and NiCo-LDH@NiFe-LDH heterostructure, the rate-determining step (RDS) changed to the formation of *OOH (*O - *OOH) with the ΔG_3 value of 1.79 eV and 1.64 eV respectively. The lower overpotential for the heterostructure signifies enhanced charge transfer and better catalytic performance. These results are consistent with the present experimental OER activity data, emphasizing the heterostructure's significance in enhancing catalytic performance.

The DFT calculations were performed to understand the enhanced performance of the Hydrogen evolution reaction (HER), focusing on the optimized adsorbed H species on the NiCo-LDH@NiFe-LDH as represented in **Figure 12c.** The Hydrogen evolution reaction (HER) is a two-step cathodic reaction in the electrochemical process that occurs on the catalyst's surface. HER involves two mechanisms, the Volmer-Heyrovsky and the Volmer-Tafel reactions.[48,49] The Volmer step involves the adsorption of hydrogen, which is expressed as $H^+ + e^- + * \rightarrow H^*$, where the * denotes Ni or Co as an active site of the surface of the catalyst. In the following Heyrovsky step, H* reacts with another proton (H^+), to form molecular hydrogen (H_2), which further releases from the surface of the catalyst, $H^* + H^+ + e^- \rightarrow H_2$.[52] To evaluate the HER activities of the proposed catalysts, we investigated the free energy pathway. The calculated Gibbs free energies (ΔG_{H*}) for NiCo-LDH, NiFe-LDH and NiCo-LDH@NiFe-LDH, respectively, are depicted in **Figure 12d.** The Gibbs free energy for the NiCo-LDH,

View Article Online
DOI: 10.1039/D5TA04519C

NiFe-LDH and NiCo-LDH@NiFe-LDH surfaces are found to be -0.58 eV, -0.41 eV and -0.33 eV, respectively. We have observed a reduction in the free energy of NiCo-LDH@NiFe-LDH heterostructure, which improves the charge transfer between the interface and modifies the electronic density of states, which weakens the adsorbed *H intermediate on the heterostructure surface and leads to the reduction of Gibbs free energy and eventually leads to accelerate the HER kinetics.

Conclusion

We developed NiFe-LDH/NiCo-LDH heterostructure via a simple hydrothermal method. Based on the aforesaid characterization, NiFe-LDH/NiCo-LDH heterostructure exhibits improved electrocatalytic OER and HER performance in alkaline conditions. The stacking of NiFe-LDH over NiCo-LDH heterostructure leads to the effective electron transfer from NiFe-LDH to NiCo-LDH, which creates a strong internal electric field between the valence band and conduction band, increasing the active surface area and conductivity for OER and HER in alkaline conditions. The heterostructure showed improved intrinsic activity as compared to other catalysts, as verified by Bode analysis and turnover frequency (TOF). Turnover Frequency (TOF) was verified for the NiFe-LDH/NiCo-LDH, showing increased TOF (0.155 sec^{-1}), which is 13 and 24 times superior to that of NiFe-LDH (0.0125 sec^{-1}) and NiCo-LDH (0.0063 sec^{-1}), respectively. The chronoamperometric (CA) analysis affirmed the long-term stability of NiFe-LDH/NiCo-LDH heterostructure, exhibiting constant performance for 60 hours under a constant potential of 1.55V vs. RHE for total water splitting. NiFe-LDH/NiCo-LDH heterostructure follows the Adsorbate enhancement mechanism (AEM) rather than the lattice oxygen mechanism (LOM) which was confirmed by the pH-dependent study. Moreover, DFT studies confirm that the NiFe-LDH/NiCo-LDH heterostructure has optimized hydrogen adsorption and desorption energy toward OER and HER catalysis. Hence,

View Article Online
DOI: 10.1039/D5TA04519C

the increased electrocatalytic activity of NiFe-LDH/NiCo-LDH, as explained by DFT simulations, highlights its importance for efficient water-splitting reactions.

Acknowledgments

H.N.D. acknowledges to CSIR-New Delhi for a Senior Research Fellowship (SRF) award. S.K. expresses gratitude to the Department of Science and Technology (DST) for CRG (Core Research Grant) funding of number # CRG/ 2021/001089 dated November 20th, 2021, having CSIR-CECRI project number GAP 22/2021. V.P. and S.C. acknowledge HRI Allahabad for the infrastructure and funding. Computational work for this study was carried out at the cluster computing facility at Harish-Chandra Research Institute (http://www.hri.res.in/cluster). Furthermore, the authors express gratitude to the Central Instrumental Facility (CIF), CSIR-CECRI, Karaikudi for providing access to the instrumental facilities. The CSIR-CECRI Manuscript number: CECRI/PESVC/Pubs/2025-030.

References:

1 P. Nikolaidis and A. Poullikkas, *Renewable and Sustainable Energy Reviews*, 2017, **67**, 597–611.

2 S. E. Hosseini, *Int J Green Energy*, 2024, **21**, 1366–1382.

3 S. Anantharaj, S. Kundu and S. Noda, *J. Mater. Chem A*, 2020, **8**, 4174–4192.

4 Q. Qian, Y. Zhu, N. Ahmad, Y. Feng, H. Zhang, M. Cheng, H. Liu, C. Xiao, G. Zhang and Y. Xie, *Advanced Materials.*, 2024, **4**, 2301608.

5 A. Roy and S. Pramanik, *Int. J. Hydrog. Energy*, 2024, **49**, 792–821.

6 N. S. Hassan, A. A. Jalil, S. Rajendran, N. F. Khusnun, M. B. Bahari, A. Johari, M. J. Kamaruddin and M. Ismail, *Int. J. Hydrog. Energy*, 2024, **52**, 420–441.

7 A. Raveendran, M. Chandran and R. Dhanusuraman, *RSC Adv.*, 2023, **13**, 3843–3876.

8 H. S. Jadhav, A. Roy, B. Z. Desalegan and J. G. Seo, *Sustainable Energy Fuels*,2019, **4**, 312–323.

9 J. Bao, X. Zhang, B. Fan, J. Zhang, M. Zhou, W. Yang, X. Hu, H. Wang, B. Pan and Y. Xie, *Angew. Chem., Int. Ed.,* 2015, **127**, 7507–7512.

10 T. Bhowmik, M. K. Kundu and S. Barman, *ACS Appl. Energy Mater.*, 2018, **1**, 1200–1209.

11 K. Xu, P. Chen, X. Li, Y. Tong, H. Ding, X. Wu, W. Chu, Z. Peng, C. Wu and Y. Xie, *J Am. Chem. Soc.*, 2015, **137**, 4119–4125.

12 Y. Wang, D. Liu, Z. Liu, C. Xie, J. Huo and S. Wang, *Chem. Comm.*, 2016, 52, 12614-12617.

13 R. Zahra, E. Pervaiz, M. Mahmood and O. Rabi, *Electrochim Acta*, 2022, **418**, 140346.

14 Z. Cai, P. Wang, J. Yang and X. Wang, *ES Energy Environ.,* 2019, **5**, 22–36.

15 D. Zhong, T. Li, D. Wang, L. Li, J. Wang, G. Hao, G. Liu, Q. Zhao and J. Li, *Nano Res*, 2022, **15**, 162–169.

16 S. Nagappan, H. N. Dhandapani, A. Karmakar and S. Kundu, *ES Mater. Manuf.*, 2021, **19**, 1–24.

17 X. Li, Z. Zhang, Q. Xiang, R. Chen, D. Wu, G. Li and L. Wang, *RSC Adv*, 2021, **11**, 12392–12397.

18 H. N. Dhandapani, D. Mahendiran, A. Karmakar, P. Devi, S. Nagappan, R. Madhu, K. Bera, P. Murugan, B. R. Babu and S. Kundu, *J. Mater. Chem. A*, 2022, **10**, 17488–17500.

19 S. Wang, T. Wang, X. Wang, Q. Deng, J. Yang, Y. Mao and G. Wang, *Int. J. Hydrog. Energy*, 2020, **45**, 12629–12640.

20 A. Karmakar, K. Karthick, S. S. Sankar, S. Kumaravel, R. Madhu, K. Bera, H. N. Dhandapani, S. Nagappan, P. Murugan and S. Kundu, *J. Mater. Chem A*, 2022, **10**, 3618–3632.

21 M. Yang, K. Wang, Y. Li, K. Yang and Z. Jin, *Appl. Surf. Sci.*, 2021, **548,** 149212.

22 J. Song, C. Wei, Z. F. Huang, C. Liu, L. Zeng, X. Wang and Z. J. Xu, *Chem Soc Rev*, 2020, **49**, 2196–2214.

23 A. Karmakar, K. Karthick, S. S. Sankar, S. Kumaravel, R. Madhu and S. Kundu, *J. Mater. Chem. A*, 2021, **9**, 1314–1352.

24 M. Li, D. Ma, X. Feng, C. Zhi, Y. Jia, J. Zhang, Y. Zhang, Y. Chen, L. Shi and J. Shi, *Small*, 2025, **21**, 2412576.

25 Y. Gui, Z. Liu, D. Ma, J. Chen, Y. Jia, S. Wu, X. Zhou, M. Li, Y. Zhang, J. Li and J.-W. Shi, *J Power Sources*, 2024, **616**, 235132.

26 Y. Zou, B. Xiao, J.-W. Shi, H. Hao, D. Ma, Y. Lv, G. Sun, J. Li and Y. Cheng, *Electrochim Acta*, 2020, **348**, 136339.

View Article Online
DOI: 10.1039/D5TA04519C

27 Y. J. Lee and S.-K. Park, *Rare Metals*, 2024, 43, 522-532.

28 F.-L. Wang, X.- Yu Zhang, J.-C. Zhou, Z.-N. Shi, B. Dong, J.-Y. Xie, Y.-W. Dong, J.-F. Yu and Y.-M. Chai, *Inorg Chem Front*, 2022, **9**, 2068–2080.

29 J. Hu, C. Zhang, L. Jiang, H. Lin, Y. An, D. Zhou, M. K. H. Leung and S. Yang, *Joule*, 2017, **1**, 383–393.

30 Y. Li, H. Xu, P. Yang, R. Li, D. Wang, P. Ren, S. Ji, X. Lu, F. Meng, J. Zhang and M. An, *Mater. Today Energy*, 2022, **25**, 100975.

31 R. Yang, Y. Zhou, Y. Xing, D. Li, D. Jiang, M. Chen, W. Shi and S. Yuan, *Appl Catal B*, 2019, **253**, 131–139.

32 H. N Dhandapani, A. Karmakar, S. S. Selvasundarasekar, S. Kumaravel, S. Nagappan, R. Madhu, B. Ramesh Babu and S. Kundu, *Inorg.Chem*., 2022, **61**, 21055–21066.

33 W. Zhao, T. Liu, N. Wu, B. Zhou, Y. Yan, Y. Ye, J. Gong and S. Yang, *Sci China Mater*, 2023, **66**, 577–586.

34 W. Y. Lim and G. W. Ho, *Procedia Eng.,* 2017, **215**, 163-170.

35 J. Zhang, H. Zhang and Y. Huang, *Appl Catal B*, 2021, **297**, 120453.

36 M. Thommes, K. Kaneko, A. V. Neimark, J. P. Olivier, F. Rodriguez-Reinoso, J. Rouquerol and K. S. W. Sing, *Pure and Applied Chemistry*, 2015, **87**, 1051–1069.

37 S. Nagappan, R. Jayan, N. Rajagopal, A. V Krishnan, M. M. Islam and S. Kundu, *Small,* 2024, 2403908.

38 G. Chen, T. Wang, J. Zhang, P. Liu, H. Sun, X. Zhuang, M. Chen and X. Feng, *Adv. Mater., 2018, **30**, 1706279.*

39 S. Wang, A. Hao and Z. Liu, *ACS Appl Nano Mater*, 2024, **7**, 28602–28611.

40 D. Duan, D. Guo, J. Gao, S. Liu and Y. Wang, *J Colloid Interface Sci*, 2022, **622**, 250–260.

41 A. C. Thenuwara, N. H. Attanayake, J. Yu, J. P. Perdew, E. J. Elzinga, Q. Yan and D. R. Strongin, *Journal of Physical Chemistry B*, 2018, **122**, 847–854.

42 H. N. Dhandapani, M. Ramasubramanian, P. Laxminarayanan, S. Singha Roy, A. De, B. R. Babu and S. Kundu, *J. Mater. Chem A*, 2025, **13**, 3506–3517.

43 H. N Dhandapani, C. Das, N. N. Ghosh, G. Biswas, B. Ramesh Babu and S. Kundu, *Inorg Chem*, 2024, **63**, 16081–16094.

44 E. M. Manohar, H. N. Dhandapani, S. Roy, R. Pełka, M. Rams, P. Konieczny, S. Tothadi, S. Kundu, A. Dey and S. Das, *Inorg. Chem*., 2024, **63**, 4883–4897.

45 H. N. Dhandapani, R. Madhu, A. De, M. A. Salem, B. Ramesh Babu and S. Kundu, *Inorg.Chem.*, 2023, **62**, 11817–11828.

46 S. Singha Roy, R. K. Sharma, A. Karmakar, S. Nagappan, B. Pathak and S. Kundu, *Applied Catalysis B: Environment and Energy.*, 2025, **371**, 125227.

47 Z. He, J. Zhang, Z. Gong, H. Lei, D. Zhou, N. Zhang, W. Mai, S. Zhao and Y. Chen, *Nat. Commun.*, 2022, **13**, 2191.

48 Z. Liu, X. Ning, A. Hao, M. F. Khan and S. Rehman, *ChemSusChem.*, 2025, 18, 1-10.

49 J. Li, G. Fu, X. Sheng, G. Li, H. Chen, K. Shu, Y. Dong, T. Wang and Y. Deng, *Advanced Powder Materials.*, 2024, **3**, 100227.

50 H. Su, C. Jin, X. Zhang, Z. Yu and X. Zeng, *Carbon Neutralization.*, 2024, **3**, 1009–1035.

51 Y. Mu, R. Ma, S. Xue, H. Shang, W. Lu and L. Jiao, *Carbon Neutralization.*, 2024, **3**, 4–31.

52 J. Greeley, T. F. Jaramillo, J. Bonde, I. Chorkendorff and J. K. Nørskov, *Nat Mater.*, 2006, **5**, 909–913.

53 J. K. Nørskov, T. Bligaard, A. Logadottir, J. R. Kitchin, J. G. Chen, S. Pandelov and U. Stimming, *J. Electrochem. Soc.*, 2005, **152**, J23-J26.

54 X. Yu, J. Zhao and M. Johnsson, *Adv Funct Mater.*, 2021, 31, 2101578.

View Article Online
DOI: 10.1039/D5TA04519C

Dr. Subrata Kundu, Ph.D, FRSC
Senior Principal Scientist
Electrochemical Process Engineering Division
CSIR – Central Electrochemical Research Institute
Karaikudi, Tamil Nadu – 630003 India
Email: skundu@cecri.res.in

June 4th 2025

To,
The Editor
Journal Materials Chemistry A
RSC Publications

Dear Editor:

Greetings! The attached file is a manuscript entitled "Hierarchal 3D-nanoflower LDHs heterojunction: A Bifunctional Electrocatalyst for water splitting" for your consideration as a 'Paper' in the highly respected *'Journal Materials Chemistry A'*.

All the data's given in the paper are available from the author upon request.

With Thanks & Best wishes,
Subrata Kundu

[**Journal's Associate Editor: Journal of Materials Chemistry A & Materials Advances (RSC); Scientific Reports (Nature Publishers); Editorial Advisory Board Member: ACS Applied Materials & Interfaces**]